Two-dimensional free-space beam steering with an optical phased array on silicon-on-insulator

J. K. Doylend*, M. J. R. Heck, J. T. Bovington, J. D. Peters, L. A. Coldren, and J. E. Bowers

Dept. of Electrical and Computer Engineering, University of California, Santa Barbara, California 93106, USA
**doylend@ece.ucsb.edu*

Abstract: We demonstrate a 16-channel, independently tuned waveguide surface grating optical phased array in silicon for two dimensional beam steering with a total field of view of 20° x 14°, beam width of 0.6° x 1.6°, and full-window background peak suppression of 10 dB.

OCIS codes: (130.3120) Integrated optics devices; (250.5300) Photonic integrated circuits.

References and links

1. N. W. Carlson, G. A. Evans, R. Amantea, S. L. Palfrey, J. M. Hammer, M. Lurie, L. A. Carr, F. Z. Hawrylo, E. A. James, C. J. Kaiser, J. B. Kirk, and W. F. Reichert, "Electronic beam steering in monolithic grating-surface-emitting diode laser arrays," Appl. Phys. Lett. **53**(23), 2275–2277 (1988).
2. D. M. Burns, V. M. Bright, S. Gustafson, and E. A. Watson, "Optical beam steering using surface micromachined gratings and optical phased arrays," Proc. SPIE **3131**, 99–110 (1997).
3. K. Van Acoleyen, W. Bogaerts, J. Jágerská, N. Le Thomas, R. Houdré, and R. Baets, "Off-chip beam steering with a one-dimensional optical phased array on silicon-on-insulator," Opt. Lett. **34**(9), 1477–1479 (2009).
4. K. Van Acoleyen, H. Rogier, and R. Baets, "Two-dimensional optical phased array antenna on silicon-on-insulator," Opt. Express **18**(13), 13655–13660 (2010).
5. D. Kwong, A. Hosseini, Y. Zhang, and R. T. Chen, "1 × 12 Unequally spaced waveguide array for actively tuned optical phased array on a silicon nanomembrane," Appl. Phys. Lett. **99**(5), 051104 (2011).
6. K. Van Acoleyen, W. Bogaerts, and R. Baets, "Two-Dimensional Dispersive Off-Chip Beam Scanner Fabricated on Silicon-On-Insulator," IEEE Photon. Technol. Lett. **23**(17), 1270–1272 (2011).
7. A. W. Fang, H. Park, R. Jones, O. Cohen, M. Paniccia, and J. E. Bowers, "A Continuous Wave Hybrid AlGaInAs-Silicon Evanescent Laser," IEEE Photon. Technol. Lett. **18**(10), 1143–1145 (2006).
8. M. N. Sysak, J. O. Anthes, D. Liang, J. E. Bowers, O. Raday, and R. Jones, "A hybrid silicon sampled grating DBR tunable laser," in *Group IV Photonics, 2008 5th IEEE International Conference on*, (Cardiff, Wales, 2008), pp. 55–57.
9. H. Park, Y.-H. Kuo, A. W. Fang, R. Jones, O. Cohen, M. J. Paniccia, and J. E. Bowers, "A Hybrid AlGaInAs–Silicon Evanescent Amplifier," IEEE Photon. Technol. Lett. **19**(4), 230–232 (2007).
10. H. Park, M. N. Sysak, H.-W. Chen, A. W. Fang, D. Liang, L. Liao, B. R. Koch, J. Bovington, Y. Tang, K. Wong, M. Jacob-Mitos, R. Jones, and J. E. Bowers, "Device and Integration Technology for Silicon Photonic Transmitters," IEEE J. Sel. Top. Quantum Electron. **17**(3), 671–688 (2011).
11. N. Le Thomas, R. Houdré, D. O'Brien, and T. F. Krauss, "Exploring light propagating in photonic crystals with Fourier optics," J. Opt. Soc. Am. B **24**(12), 2964–2971 (2007).
12. V. A. Sychugov, A. V. Tishchenko, B. A. Usievich, and O. Parriaux, "Optimization and control of grating coupling to or from a silicon-based optical waveguide," Opt. Eng. **35**(11), 3092–3100 (1996).

1. Introduction

Optical phased arrays enable free-space beam steering without moving parts, making them desirable for robust point-to-point free-space communications, Light Detection and Ranging (LIDAR), and optical memory. Chip-scale optical phased arrays have been demonstrated using tunable gain elements [1] and phase tuning [2], and phased arrays composed of waveguide surface gratings in silicon-on-insulator (SOI) have also been demonstrated with a steering range of 2.3° x 14° using a single thermo-optic phase tuner together with wavelength tuning [3,4]. While the approach demonstrated by Acoleyen *et al.* is both CMOS-compatible and elegant in its simplicity, there is no means of actively compensating for accumulated phase errors between individual channels due to on-chip propagation and thermal cross-talk, thus resulting in undesirable off-axis peaks and limited tuning range. Phase tuning of the

#153199 - $15.00 USD Received 22 Aug 2011; revised 21 Sep 2011; accepted 30 Sep 2011; published 18 Oct 2011

individual channels provides a solution to these problems; such an approach has been used to demonstrate 1-dimensional beam steering in a silicon slab [5]. Also of note is an alternate technique in which an entirely passive device was used to raster a beam across the far field using wavelength alone [6], thus avoiding phase tuning elements altogether at the cost of a relatively wide beam in the far field (4°) and no means of arbitrarily shaping the wavefront. The use of SOI is significant because it is compatible with standard CMOS fabrication techniques; furthermore, with the advent of tunable optical sources [7, 8] and amplifiers [9, 10] using hybrid integration of IIII-V gain materials with silicon rib waveguides, the prospect of a self-contained steerable free-space optical source becomes possible.

In this work we demonstrate a 16-channel optical phased array in SOI in which the phase of each channel is individually controlled to achieve free-space beam steering in two dimensions across a 20° x 14° field of view, far field beam width of 0.6° x 1.6°, and 10 dB background peak suppression. The phase tuning was accomplished thermo-optically using resistive heaters in the vicinity of the waveguides. Phase errors and background peaks were minimized by an optimization algorithm using feedback from an infrared camera which recorded the far field image in real time; a lookup table of solved phase settings was then used to steer the beam arbitrarily without the need for real-time feedback. In this manner thermal crosstalk and phase errors were circumvented so as to achieve arbitrary two dimensional beam pointing within the field of view.

2. Design and fabrication

Rib waveguides of 1 μm width were patterned via photolithography in SOI and dry-etched to a depth of 280 ± 20 nm. The SOI has 500 nm top silicon thickness and 1 μm buried oxide. Multi-mode interferometer (MMI) 1x2 couplers were used to split the beam into 16 channels. Surface gratings were defined via e-beam lithography and etched to a depth of 75 nm. Resistive heaters of 470 μm length for thermo-optic tuning were fabricated by e-beam deposition and lift-off of a 72 nm / 75 nm nickel-chrome-gold metal stack directly on the silicon surface. The heaters were offset 6.5 μm from the rib waveguides so as to avoid excess loss due to metal optical absorption at the expense of thermal tuning efficiency. The waveguides in this phase-tuning region of the device were spaced 100 μm apart, of which 79 μm was etched entirely to the buried oxide to enhance thermal isolation. The grating array had 50% duty cycle, 3.5 μm lateral waveguide spacing, 200 μm length, and full width (i.e. the grating grooves completely spanned each waveguide). The propagation length from the input to the grating was approximately 4 mm. A schematic picture of the device is shown in Fig. 1.

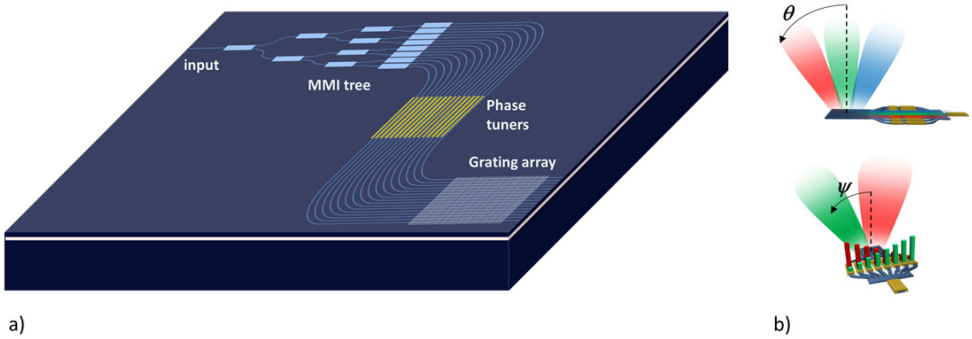

Fig. 1. a) Schematic diagram of the 16-channel grating array with independently tuned channels for 2-dimensional beam steering. A multi-mode interferometer (MMI) tree split the input into 16 channels which were then independently phase tuned and coupled to a grating array. Beam steering in the longitudinal axis θ was accomplished via wavelength tuning while beam steering in the lateral axis ψ was accomplished by phase tuning. b) Schematic diagrams illustrating the respective orientations of the longitudinal axis θ and the lateral axis ψ.

#153199 - $15.00 USD Received 22 Aug 2011; revised 21 Sep 2011; accepted 30 Sep 2011; published 18 Oct 2011

The small grating etch depth relative to the overall rib waveguide dimensions was chosen to reduce the grating strength, thus increasing the propagation length over which the guided mode was outcoupled in order to maintain a narrow beam in the far field along the longitudinal axis. Solitary waveguide surface grating test structures with a variety of duty cycles and grating widths (i.e. width of the grating groove within the rib waveguide) were fabricated alongside the 16-channel device in order to evaluate the feasibility of incorporating chirp/apodization into future grating array devices. Scanning electron microscope images of the grating array, a grating test structure, and an optical microscope image of the phase tuners are shown in Fig. 2.

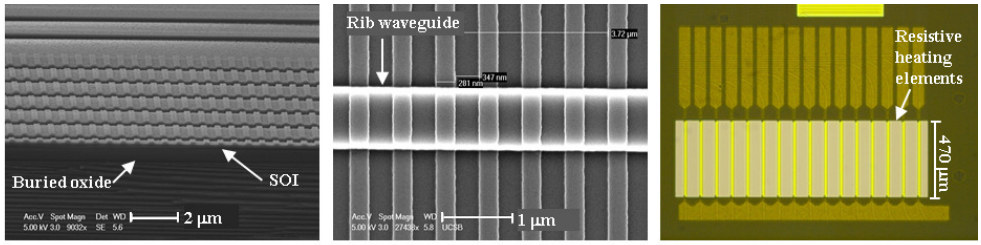

Fig. 2. Scanning electron microscope images of (a) the grating array cross-section, (b) a single surface waveguide grating test structure, and (c) optical microscope images of the thermo-optic phase tuners.

3. Passive grating characterization

The far field output was characterized using a high-numerical-aperture aspheric lens (NA = 0.83, effective focal length = 15 mm) to image the far field into the Fourier plane and two additional lenses (effective focal lengths 180 mm and 60 mm) to magnify and focus the beam onto an infrared camera (320x256 pixels, 25 μm pitch); this system has far field resolution of 0.3° at normal outcoupling. The maximum longitudinal outcoupling angle measurable by the system (without tilting the lens tube relative to the chip surface) is 39°; the maximum measurable angle in the lateral direction is 33°. A polarization controller was used to align the polarization along the TE axis and a polarizer mounted in front of the camera was used to filter out any remaining TM polarized scattering; all measurements described in this work are for TE polarized input light. The 180 mm focal length lens was attached via a rotating mount such that near field images of the grating could be collected and then the lens could be reinserted for far field images. This characterization technique follows the approach presented by Thomas *et al.* [11] and enabled the system to be focused on the grating array (using the near field image for guidance) prior to collecting far field data. This system will henceforth be referred to as the "Fourier imaging system".

#153199 - $15.00 USD Received 22 Aug 2011; revised 21 Sep 2011; accepted 30 Sep 2011; published 18 Oct 2011

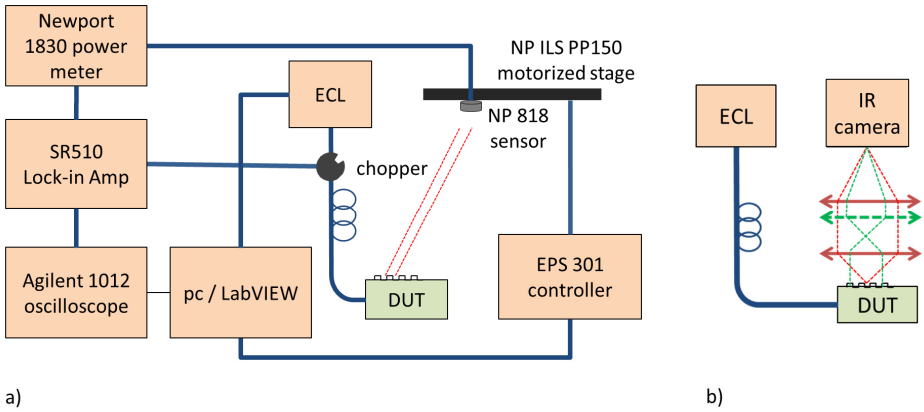

Fig. 3. a) Beam profiler measurement system, and b) Fourier imaging system with removable lens for near field imaging. The removable lens is shown in green together with the associated far field ray traces, while the non-removable lenses are shown in red with the associated near field ray traces. ECL = external cavity laser; DUT = device under test.

A second characterization system consisting of a Newport 818 photodetector mounted on a Newport ILS PP150 motorized stage at a distance of 14.7 cm from the chip surface and translated across the far field was used to profile the beam and calibrate the Fourier imaging system. A schematic of each characterization system is shown in Fig. 3.

Test structures consisting of individual gratings fabricated on isolated waveguides were characterized to assess wavelength tuning and longitudinal beam width. The longitudinal emission angle θ is given by Eq. (1):

$$\sin\theta = \frac{n_{eff}\Lambda - \lambda_0}{\Lambda} \tag{1}$$

where n_{eff} is the effective index of the waveguide within the grating for λ_0, Λ is the grating pitch, and λ_0 is the free-space wavelength.

The longitudinal optical far field emission profile of a test grating with 600 nm pitch measured using the beam profiler is shown in Fig. 4 together with corresponding far field images captured using the Fourier imaging system and a plot of the longitudinal emission angle as a function of wavelength both for the 16-channel grating array and a corresponding test structure. The simulated output was obtained from Eq. (1) using the calculated effective index of the waveguide within the grating. For wavelengths from 1525 nm – 1625 nm, the tuning efficiency was measured to be 0.14 ± 0.01 °/nm, matching the value calculated from RSoft BeamPROP simulations. An offset of 4° between the measured and simulated outcoupling was observed and attributed to the effects of trenching, non-vertical sidewalls, and etch depth variation. The results of the Fourier imaging measurement matched those of the beam profile measurement, thus experimentally validating the former.

#153199 - $15.00 USD Received 22 Aug 2011; revised 21 Sep 2011; accepted 30 Sep 2011; published 18 Oct 2011

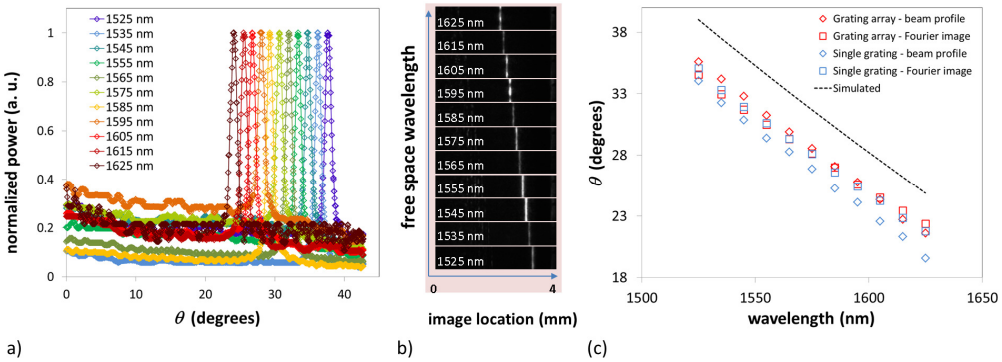

Fig. 4. (a) Normalized optical output profile in the far field measured using the beam profiler; (b) Far field images captured using the Fourier imager for wavelengths from 1625 nm (top) to 1525 nm (bottom); (c) Plot of the longitudinal beam angle in the far field measured for an individual grating (blue) and a 16-channel grating array (red) using both the Fourier imaging system (square markers) and beam profiler (diamond markers), with the simulated output calculated from the Bragg equation shown for comparison.

The ability to chirp individual gratings or to apodize the grating array can be a valuable means of optimizing efficiency and beam shape; grating width and duty cycle are parameters which can be adjusted for this purpose. However, since the far field emission angle is affected not only by wavelength but also by variation in the effective index according to Eq. (1), the variation in output angle as a function of grating duty cycle and width (i.e. the width of the grating grooves relative to the rib waveguide – see Fig. 5b) can be a concern since it necessarily introduces a spread of outcoupling angles in the far field. Accordingly the angular variation of the output as a function of duty cycle and grating width was characterized using single-grating test structures. A plot of the angular deviation with respect to each parameter is shown in Fig. 5 together with SEM images of gratings with varying width and duty cycle. As expected, $\Delta\theta$ decreased with duty cycle due to the decreasing effective index of the mode with a larger fraction of the rib etched away and decreased for wider etched grating trenches. Total variation of >2° in the outcoupling angle was observed for duty cycles ranging from 20% - 80%, and > 1.5° variation was observed for grating widths ranging from 100 nm – 900 nm. Accordingly, using these parameters as a means of chirping and/or apodizing would involve a significant tradeoff due to concomitant increases in beam width.

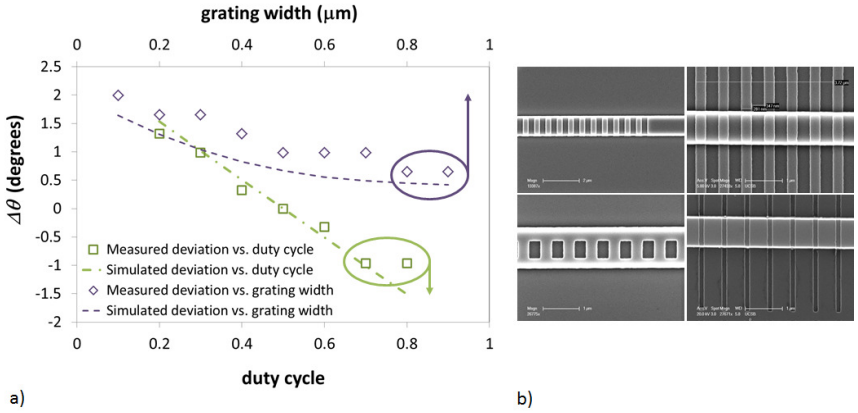

Fig. 5. Plot of the longitudinal angular deviation in the far field (calculated relative to the output for 50% duty cycle and full width (i.e. width extending across the entire array of test structures) measured and simulated as a function of grating width and duty cycle. Shown to the right are SEM images of a 50% duty cycle grating with 0.9 μm width (upper left), 400 nm width (lower left), 50% duty cycle full width (upper right), and 20% duty cycle full width (lower right).

#153199 - $15.00 USD Received 22 Aug 2011; revised 21 Sep 2011; accepted 30 Sep 2011; published 18 Oct 2011

For a uniform grating the longitudinal beam width in the far field is determined by the propagation length over which power is emitted. The scattering profile of each single-grating test structure was measured from near field images of the optical emission, fitted to an exponential decay, and used to calculate beam width (full-width half-maximum, or FWHM) in the far field by numerically integrating the associated Fourier transform. These calculated results are plotted for a selection of duty cycles and grating widths in Fig. 6 together with the beam width directly measured in the far field using the Fourier imaging system. Theoretical values calculated from the propagation loss simulated using RSoft FullWAVE are shown for comparison.

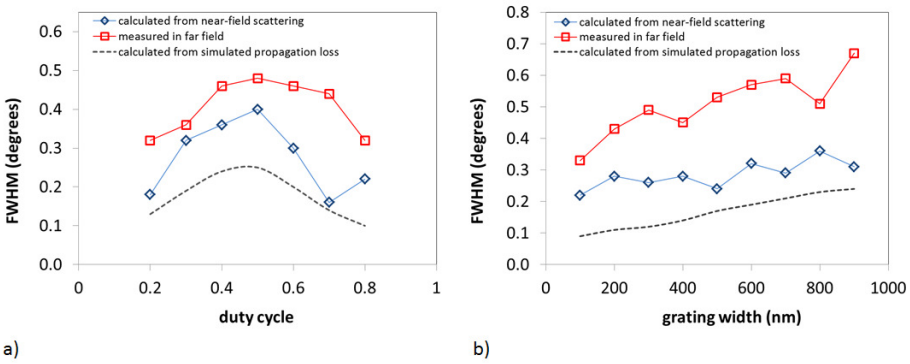

Fig. 6. Plots as a function of grating duty cycle (a) and width (b) of the longitudinal beam width (FWHM) in the far field calculated from the scattered power distribution in the near field (blue) and measured directly from the far field image (red) at 1555 nm.

The grating strength increased as duty cycle approached 50%, yielding a smaller effective grating length and thus a larger beam width in the far field. Similarly, the grating strength increased with grating width, reducing the effective grating length and thus spreading the beam in the far field. The discrepancy between FWHM calculated from the near field images and measured directly in the far field was attributed to mode evolution within the grating, resulting in a spread of output emission angles and hence a larger than expected beam width. It should be noted that the measured far field beam width is also limited by the angular measurement resolution of the system (0.2° per pixel at θ = 31°). The disparity between the simulated and actual beam width also suggests additional scattering mechanisms within the grating (e.g. sidewall roughness).

3. Phase tuned grating array characterization

While beam control in the longitudinal axis θ was controlled with wavelength, control in the lateral direction was accomplished with a phased array. For a regular emitter array, the lateral direction ψ of the beam is determined according to Eq. (2):

$$\sin\psi = \frac{\lambda_0 \phi}{2\pi d} \tag{2}$$

where ϕ is the uniform phase increment between emitters, and d is the emitter spacing. In practice, however, phase errors are introduced by differences in effective path length between channels due to wavelength bends and process variation across the chip. To correct for these phase errors, a resistive heater was added in the vicinity of each waveguide so as to permit individual thermo-optic phase tuning of each channel.

The phase tuning efficiency of a single element was measured using a Mach-Zehnder interferometer (MZI) test structure with the same waveguide profile and phase tuners used in the 16-channel grating array. The efficiency was found to be (215 ± 15) mW/π. In order to

#153199 - $15.00 USD Received 22 Aug 2011; revised 21 Sep 2011; accepted 30 Sep 2011; published 18 Oct 2011

provide 430 mW per channel as required to reach a full 2π tuning range, an ILX 3916 laser driver array with modulation inputs driven by a National Instruments analogue output data acquisition card via a custom-built buffer array was used. The thermo-optic tuners were fabricated with a resistance of (65 ± 5) Ω such that each could be driven past 500 mW without exceeding the laser driver voltage limit of 7.5 V.

Thermal crosstalk between channels was measured by recording the resistance of each tuning electrode in the array at steady state while a single channel was subjected to high thermal power. The dependence of tuner resistance on temperature was determined separately by fabricating identical tuners on bulk silicon and measuring their resistance and the temperature of the substrate while slowly heating the substrate. A plot of the relative temperature thus measured across the tuning array with 15 of the 16 channels each driven to 30 mW while a single channel near the center (channel 9) was driven at higher thermal power is shown in Fig. 7.

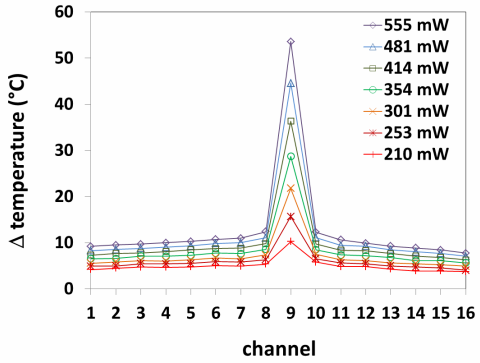

Fig. 7. Relative thermal gradient across the 16-channel array when 15 channels were driven at 30 mW and a single central channel was driven at higher thermal powers. Temperatures (relative to the corresponding values when all channels were driven at 30 mW) were calculated from the change in resistance of each tuner; the relationship between resistance and temperature for the tuners was calibrated separately using a thermocouple to record the temperature of a bulk silicon substrate on which identical tuners had been fabricated.

It is apparent from Fig. 7 that crosstalk between channels is significant, with all channels heated by several degrees in response to power injected on a single channel. Since individual channels were separated by 79 μm wide trenches etched through the top silicon to the buried oxide, this suggests that injected thermal power heats the whole top silicon layer above the buried oxide as well as affecting adjacent channels via heat transfer along the axis of the waveguide particularly around the beginning and end of the thermal isolation trenches. This problem may be alleviated in future by using a thinner buried oxide and by etching holes through the buried oxide and depositing metal at each end to form thermal shunts between the top silicon layer and the substrate.

While phase errors might be eliminated for a given beam angle using a particular phase vector applied to the thermo-optic tuners for each wavelength, a different beam angle requires a new tuning vector determined not only by Eq. (2) but also by the thermal crosstalk. It was therefore impractical, within this configuration, to control the beam output using Eq. (2) to predict the 16-element thermal tuning vector required for a given beam angle. Instead a brute-force hill-climber algorithm implemented in NI LabVIEW code was used to solve for the optimal tuning vector along each desired beam direction, with the Fourier imaging system providing far field feedback. The algorithm operated by setting five closely spaced drive currents on a given channel and comparing the far field distribution for each by parsing the image from the infrared camera to calculate R, where R is the ratio of the power $P(\psi_0,\theta_0)$ (i.e. power measured in the vicinity of the desired angles ψ_0 and θ_0) to the overall power $\int P(\psi,\theta_0)d\psi$ collected within the total field of view near longitudinal angle θ_0. The algorithm

#153199 - $15.00 USD Received 22 Aug 2011; revised 21 Sep 2011; accepted 30 Sep 2011; published 18 Oct 2011

calculated $R(i,\psi_0,\theta_0)$, $\partial R/\partial i$, and $\partial^2 R/\partial i^2$ using a polynomial fit, evaluated a truth table to decide in which direction and how far to step the drive current on the given channel, and then proceeded to the next channel. A flowchart illustrating these steps is shown in Fig. 8.

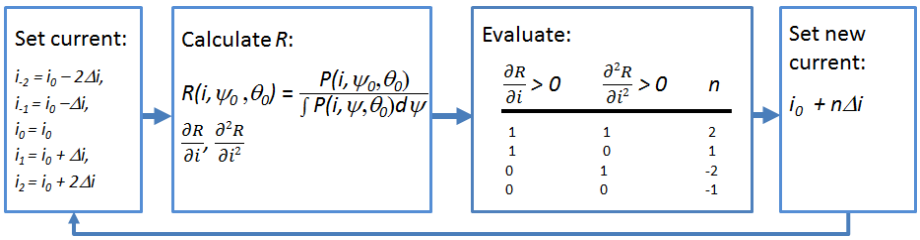

Fig. 8. Hill-climber algorithm implemented in NI LabVIEW and used to optimize the phase tuning of the 16-channel grating array for beam outcoupling at a given lateral angle ψ using feedback from the Fourier imaging system.

Using this automated optimization routine together with real-time feedback from the Fourier imaging system, phase tuning solution sets with background suppression of 10 dB were obtained for points at 1 degree spacing in each axis across a 14° (θ axis) by 20° (ψ axis) field of view. The algorithm generally required less than 100 iterations of the full tuning array to reach a solution; the iterative speed was limited by the 60 Hz refresh rate of the infrared camera such that 1.3 seconds was required to evaluate and adjust the full 16-element phase vector at 5 points per channel. Total solution time for each point was therefore typically less than 2.5 minutes although certain locations within the field of view required considerably longer to converge.

Representative plots of the beam profile at $\psi = 0°$, $\theta = 31°$ (i.e. 1555 nm) as seen without phase tuning and as solved by this system are shown in Fig. 9 along with theoretical profiles and the corresponding sections of the far field images.

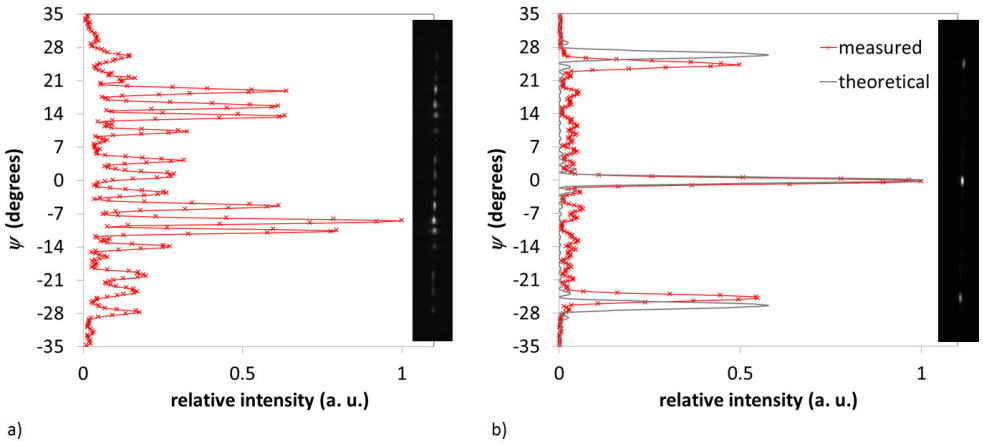

Fig. 9. Beam profile in ψ axis and corresponding sections of the far field image for a wavelength of 1555 nm (a) without phase tuning and (b) with phase tuning after applying the optimization algorithm. The 2° discrepancy between measured and theoretical side lobe location is attributed to lens Seidel aberrations.

The theoretical profile was attained by summing the far field contributions from each emitter assuming an emission amplitude function corresponding to the calculated mode profile at the grating etch depth. The measured beam width (FWHM) along ψ was 1.6°. It should be noted that the location of the secondary peaks at $\psi = \pm 26°$ was determined by the spacing between array elements while their height was determined by the width of each array element. For beam pointing applications where the ability to collect the output at a single

#153199 - $15.00 USD Received 22 Aug 2011; revised 21 Sep 2011; accepted 30 Sep 2011; published 18 Oct 2011

emission angle is required, the total field of view over which a solitary beam can be swept is limited by the secondary peak spacing; for the device described here, the maximum total field of view was ±10° in order to prevent secondary peaks from encroaching on the field of view. It is therefore apparent that for a given number of channels there is a tradeoff in the ψ axis between beam width (ideally as small as possible) and total field of view (ideally as large as possible) since increased spacing between adjacent gratings reduces both the beam width and the secondary peak spacing.

The phase solution set obtained for the entire field of view using the algorithm/feedback technique described above was then used to generate a look-up table (LUT) such that the beam could be pointed arbitrarily without further need for real-time feedback. Profiles of the beam in the ψ axis for alignment at 1° increments across the field of view are shown in Fig. 10, and 3D plots of the beam measured at the corners and center of the field of view are shown in Fig. 11.

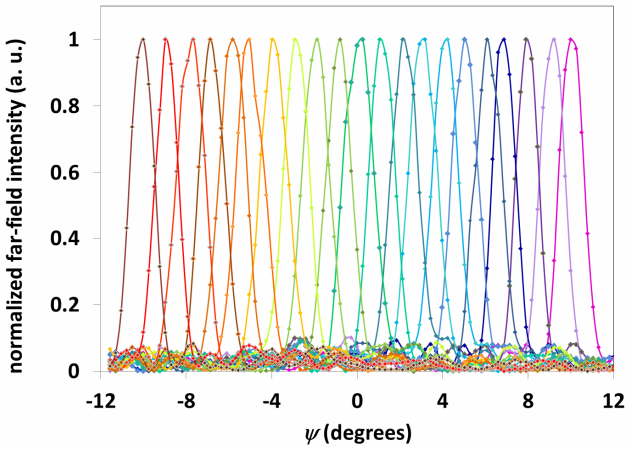

Fig. 10. Measured beam profiles at 1555 nm wavelength as the beam was swept across the field of view in the ψ axis at 1° increments.

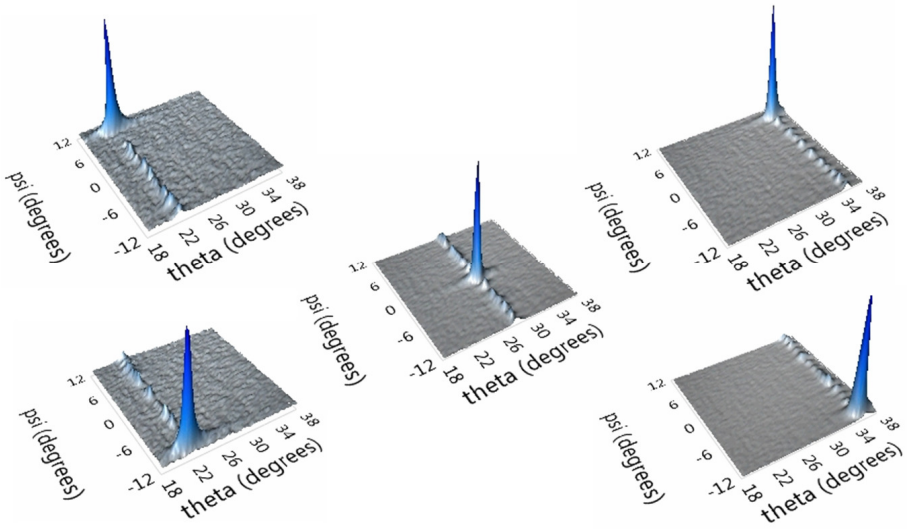

Fig. 11. Plots of the 2D beam profiles at the corners and centre of the field of view located using the LUT. The field of view was chosen so as to exclude the secondary peaks.

#153199 - $15.00 USD Received 22 Aug 2011; revised 21 Sep 2011; accepted 30 Sep 2011; published 18 Oct 2011

The optical efficiency of the device was measured by using the lookup table to point the beam at the Newport 818 photodetector in the far field. The Newport 818 photodiode has a 3 mm diameter aperture - corresponding to 0.8° at a distance of 147 mm and θ = 35°; the photodiode aperture therefore limited the portion of the beam collected in the ψ axis. However a comparison of the measured peak power (−41.2 dBm for fiber launch power of −13 dBm) with the known photodiode aperture and measured beam width of 1.6° in the ψ axis suggests total beam power of −38.4 dBm (beam width in the θ axis was 0.7°, and therefore not significantly apertured by the photodiode). On-chip waveguide propagation loss and fiber-to-chip facet coupling loss were measured via the Fabry–Pérot transmission fringes of a straight waveguide test structure and found to be 3.0 ± 0.2 dB/cm and 10.1 ± 0.2 dB respectively using 1.7 μm spot size lensed fiber. Since on-chip propagation length prior to the grating array was 4 mm, the grating efficiency (defined as the quotient of total power in the desired far field beam and on-chip waveguide-coupled power) was calculated to be −14.1 ± 0.2 dB. Of this, theoretical coupling to the side lobes was calculated to account for 6.4 dB and downward emission into the substrate was calculated to account for 5.8 dB. The former can be addressed in future devices by increasing the rib waveguide width in order to suppress side lobes; the latter may be improved by optimizing the buried oxide thickness [12]. The remaining 1.9 dB was therefore due to excess loss within the 16-channel MMI tree and the grating array.

4. Conclusion

A 16-channel optical phased array fabricated in SOI with independently phase-tuned channels has been fabricated and shown to achieve free-space beam steering across a 20° x 14° field of view with far-field resolution of less than 1°, and background suppression of more than 10 dB. The effect of duty cycle and grating width on far field beam direction and size were characterized and shown to introduce significant alteration in regard to both.

An algorithm using feedback from far field images of the beam was applied to the 16-channel device to solve for phased array solutions at each beam direction in the field of view, and these solutions were then incorporated into a lookup table such that the beam was steerable in two dimensions without feedback. This approach shows promise as a means of achieving rapidly scanned beams in two dimensions for applications such as LIDAR, free space communications and optical memory.

Acknowledgements

The authors thank Pietro Binetti, Weihua Guo, Chad Althouse, Ben Curtin, Bill Mitchell, and Scott Rodgers for useful discussions. This research was supported by the DARPA Sweeper program, grant #HR0011-10-2-0003. Jonathan Doylend's work was supported in part by a Natural Sciences and Engineering Research Council of Canada Post-doctoral Fellowship.

#153199 - $15.00 USD Received 22 Aug 2011; revised 21 Sep 2011; accepted 30 Sep 2011; published 18 Oct 2011